DIRECT-CURRENT DISCHARGE BETWEEN A METAL ANODE AND A LIQUID NONMETALLIC CATHODE

S. Yu. Petryakov[a]**, D. N. Mirkhanov**[a]**, A. F. Gaisin**[b,*]**,**
R. Sh. Basyrov[a]**, and N. F. Kashapov**[c]

UDC 537.528

Abstract: The characteristics and mathematical modeling of the behavior of a low-temperature direct-current electric discharge plasma ignited between an aluminum anode and an electrolytic cathode (3% NaCl solution in purified water) at atmospheric pressure are investigated. The discharge is ignited by immersing the metal anode into the electrolytic cathode. The types and forms of plasma structures generated in the interelectrode gap are considered. The results of high-speed recording of the discharge breakdown and combustion are presented. The electrophysical parameters of the discharge, including pulsations and current/voltage fluctuations are studied. The emission spectroscopy method is used to determine the discharge emission spectrum, plasma composition, electron concentration, and temperature of heavy plasma components. The heat patterns of the surface of liquid nonmetallic and metallic electrodes in the discharge combustion zone are considered. The results of numerical simulation of electric field strength and the initial stage of the discharge are presented.

Keywords: low-temperature plasma, electric discharge, plasma–liquid systems, numerical methods.

INTRODUCTION

The study of low-temperature discharge plasma with liquid nonmetallic electrodes is a rapidly developing interdisciplinary field of research [1]. In plasma–liquid systems, discharges are generated by direct or alternating current in the interelectrode space, while liquid is used as one of the electrodes. As a rule, salt solutions of various concentrations in distilled, industrial, or purified water are used as a liquid electrode. A discharge is ignited in gas-discharge chambers with electrodes of various configurations. The most common methods for igniting a discharge are immersing a metal electrode into an electrolyte and placing the metal electrode at a certain distance from the electrolyte surface [2, 3].

Interest in plasma–liquid systems is due to the fact that this field of research connects three systems describing the physics of processes in plasma (gas discharge), liquid (nonflowing and flowing electrolytes), and gaseous (ambient air) phase states. These systems comprise more than 50 charged or neutral atomic and molecular particles that react with each other and affect the energy balance in the discharge [4]. The complexity of numerical calculations

[a]Kazan National Research Technical University named after A. N. Tupolev, Kazan, 420111 Russia; serioga_com@mail.ru; mirhanov@list.ru; rafikbasyrov@mail.ru. [b]Joint Institute for High Temperatures, Russian Academy of Sciences, Moscow, 125412 Russia; *almaz87@mail.ru. [c]Kazan (Volga region) Federal University, Kazan, 420008 Russia; kashnail@gmail.com. Translated from Prikladnaya Mekhanika i Tekhnicheskaya Fizika, Vol. 63, No. 5, pp. 20–32, September–October, 2022. Original article submitted October 27, 2021; revision submitted December 7, 2021; accepted for publication December 27, 2021.

*Corresponding author.
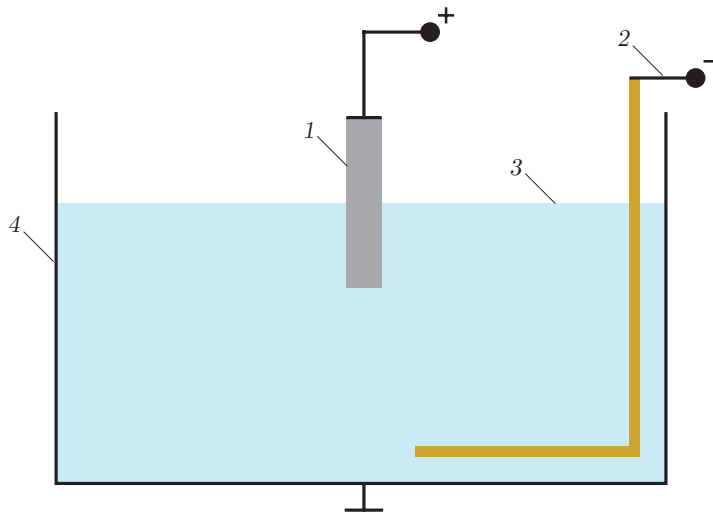
Fig. 1. Gas-discharge chamber: (*1*) aluminum anode; (*2*) copper plate for negative potential in the electrolyte; (*3*) electrolyte (3% NaCl solution in purified water); (*4*) electrolytic cell.

is due to the fact that the mathematical model of plasma–liquid systems may include more than 30 equations, depending on the number of particles taken into account. The results obtained in this case are in poor agreement with the experimental data, which makes it difficult to create a unified classification of plasma–liquid systems, similar to the well-known classification of discharges in the case of using solid electrodes (spark, continuous, glow, corona, etc.) [5]. At the same time, one of the directions for systematizing discharges with liquid electrodes is their classification according to elementary processes, so it becomes an urgent task to create mathematical models based on them, whose computational results are qualitatively and quantitatively consistent with experimental data.

At the same time, plasma–liquid systems are used to solve various applied problems in mechanical engineering, metalworking, medicine, and the space industry. Researchers also work on the possibility of using discharges with liquid electrodes in treatment of products which have complex geometry of external and internal surfaces and which are manufactured using traditional production methods (stamping, casting, etc.) [6–8] and additive methods of laser sintering of metal powders [9]. There are many works describing the studies performed using plasma–liquid systems for producing fine metal powders [10], obtaining nanoparticles [11, 12], coating products [13, 14], analyzing the particle concentration in a liquid [15, 16], creating plasma-chemical reactors [17, 18], and for sterilizing or purifying solids, water, and air [19]. The use of these systems is due to a wide variety of configurations of gas-discharge chambers, regimes and parameters of ignition and discharge combustion, and plasma-chemical processes associated with matter and charge transfer at the interface [20, 21].

The purpose of this work is to study the properties of the resulting discharge when an aluminum anode is immersed in an electrolytic cathode at atmospheric pressure. Its electrical, spectral, and thermal parameters are of particular interest. In order to interpret the detected effects, numerical experiments are carried out in which the electric field strength and the initial stage of the discharge are simulated.

1. EXPERIMENTAL DEVICE

Figure 1 shows the schematic of a gas-discharge chamber for ignition and preservation of a discharge between an aluminum anode and an electrolytic cathode (3% NaCl solution in purified water) at atmospheric pressure.

A cylindrical rod made of AMTs-40 aluminum alloy is used as a metal anode. The anode is immersed in the electrolyte and, with the help of an automatic manipulator, is moved in a vertical plane over a distance of 30 mm. A negative potential is supplied by immersing a copper metal plate in the electrolyte. A thermostat is used to control the electrolyte solution temperature in a tray. The electrolyte temperature is controlled using

a refrigeration circulation cooler. The electrolyte in the tray is renewed using the electrolyte supply and pumping system. The solution is purified using a coarse filter in the system. Electrolyte vapors are removed from the discharge study area using a stationary air extraction system and a fan.

The experimental device is equipped with a high-voltage generator with a power of 40 kW, a variable voltage of up to 4 kV, and a nominal current of up to 10 A, which supplies current in the discharge. This device also consists of diagnostic and auxiliary equipment. The power generator converts and controls the system voltage. The generator consists of high- and low-voltage adjustable blocks, which ensure necessary voltage and current ranges. The device is grounded. The resulting values of the current and voltage are transmitted from the source console to the control computer and controlled by the operator.

The experimental studies of the discharge are carried out at the following parameter values: voltage $U = 100$–500 V, anode current density $j_a = 0.2$–0.6 A/cm^2, pressure $p = 10^5$ Pa, electrolyte temperature $T = 10$–25°C, anode diameter $d_a = 5$ mm and electrolyte conductivity $\sigma = 0.10$–0.12 $\Omega^{-1}\cdot$cm^{-1}.

The problems presented in this paper are solved using modern diagnostic equipment and various methods.

The processes occurring in the discharge combustion zone and the plasma structures formed in this case are recorded on video using a Casio EX-F1 high-speed video camera. Due to the high rate of the processes occurring in the discharge combustion zone, the video recording speed is chosen to be 1200 and 600 fps. The video camera mounted on a tripod at a distance of 300 mm from the discharge zone transmits the received information to the computer. The received data are processed using the HX Link and Movavi Video Editor 14 Plus software. At the same time, the anode and cathode spots on the surface of liquid and metal electrodes are investigated in detail using an SP-52 microscope.

The discharge plasma emission was analyzed by emission spectroscopy using a PLASUS EC 150201 MC fiber-optic spectrometer. The discharge emission was recorded using a collimator to fix light beams in a wavelength range of 195–1105 nm. The collimator was connected to the discharge combustion zone at a distance of 100–200 mm. The hardware function of the system was tested using light emission from a SIRSh 6-100 lamp. The hardware width is assumed to be equal to the width of the minimum single and narrowest lines of the spectrum, $\Delta\lambda_{\mathrm{G}} = 1$ nm. The studied emission was accumulated in the entire volume of the generated discharge, so the plasma composition and the plasma components were estimated with no reference to a specific point. The resulting data were analyzed by comparing the studied spectrum with the database of the National Institute of Standards and Technology (USA). The vibrational and rotational temperatures of the heavy plasma component were determined by comparing the experimentally recorded molecular spectrum with the spectrum obtained in the computational model using the LIFBASE and SPECAIR 2.2.0.0 software.

The temperature distribution of the surface of the metallic and electrolytic electrodes during the discharge combustion is analyzed using a FLIRA6500SC thermal imaging camera whose detector has a spatial resolution of 640×512 pixels in an operating range of spectral lines of 3.6–4.9 μm. The thermal imager ensures that the temperature on the electrode surface is fixed within a tested range of 4–2400°C. A multiwavelength pyrometer is used to test the thermal imaging camera. The use of a pyrometer is due to the fact that an oxide film and a fire scale can form during the discharge combustion, thereby causing errors in temperature measurements. The processing of the obtained values is carried out using the ALTAIR v5.91.010 software.

Pulsations and fluctuations of the current and voltage of the discharge are studied using the GDS-806S and GOS-6030 digital oscilloscopes. In order to ensure that the electrophysical parameters at the time of ignition are controlled and that the discharge is preserved, a device is connected to the oscilloscopes for recording the optical emission of the discharge on photodiodes with a microcircuit.

The discharge is modeled in ANSYS FLUENT 16.2. The flowing of the current in an electrolytic cell with a grounded conductive bottom is considered. Geometric constructions are used to construct a $100 \times 100 \times 40$-mm computational domain. The problem is solved using the finite element method, and the computational domain is divided into elements shaped as tetrahedra. The model is a liquid–air–vapor three-component system. The presence of ions in the electrolyte is taken into account for the liquid phase, and the processes of evaporation, condensation, and interfacial heat transfer are taken into account for the vapor–gas phase. The system describing the dynamics of a vapor–gas medium and a liquid includes the equations of mixture continuity, of motion (momenta), of energy, and of the electric field potential.

(a)   (b)

5 mm   5 mm
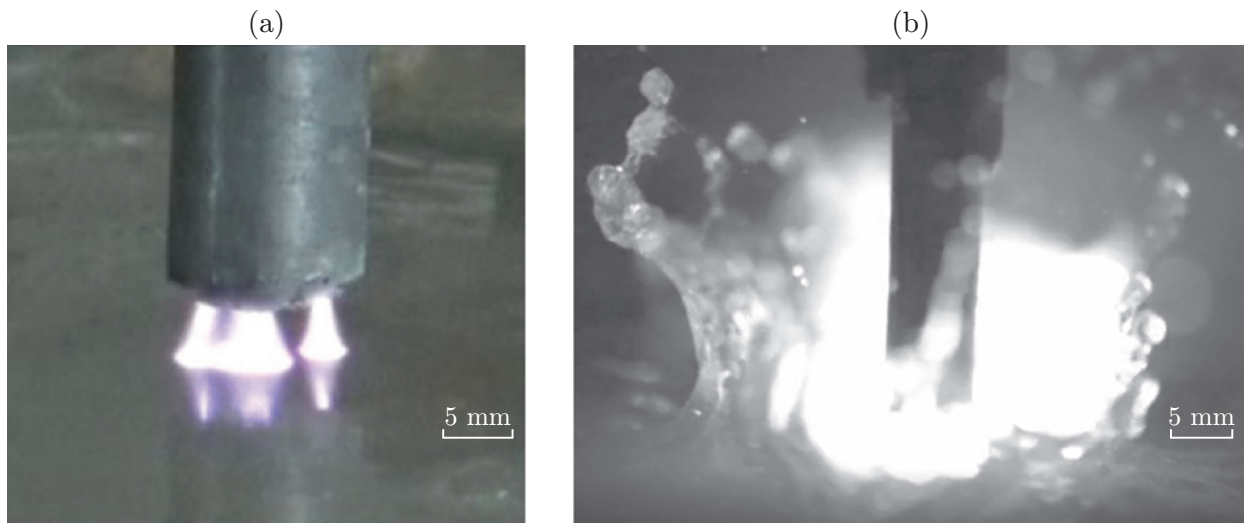
Fig. 2. Electric discharge combustion process in the region between the aluminum anode and the electrolytic cathode at $p = 10^5$ Pa and $d_a = 5$ mm: (a) $U = 400$ V and $I = 0.55$ A; (b) $U = 800$ V and $I = 8$ A.

2. DISCUSSION OF THE RESULTS

The study of discharge initiation as a result of contact between an aluminum anode with a diameter $d_a = 5$ mm and the surface of an electrolytic cathode shows that applying voltage in a range of 100–170 V results in the electrolyte evaporation process at the electrode contact boundary with the formation of vapor–air bubbles of various diameters. The current flowing in the circuit triggers the Joule heat release from the metal anode surface and the release of dissolved substances from the electrolyte, which is typical for electrolysis. The electrolysis process is determined by the transfer of electric current in the liquid and the type of discharge of the electrolyte ions contained in the solution. It is possible to change the nature of the electrode processes by changing the composition, concentration, and temperature of the electrolyte. At the same time, there is no breakdown because the power deposited in the discharge remains insufficient to ionize the vapor–air medium and initiate an electron avalanche.

As the voltage rises from 200 to 400 V, the intensity of the processes occurring in the interelectrode gap increases and the solution around the aluminum anode begins to boil (Fig. 2). Inside the electrolyte, a phase separation boundary appears, and a vapor–air shell is formed around the anode. At some time point, the electric field strength reaches values sufficient to trigger the processes that initiate the breakdown of the gas gap between the electrodes. The breakdown results in microdischarges shaped as a truncated cone and located at the interface between the media. The top of this cone rests on the surface of the aluminum anode, and its base rests on the surface of the electrolytic cathode (Fig. 2a). Electric discharges are formed as current pulses in a range $I = 0.2$–1.8 A. At the same time, the formation and preservation of the discharge are accompanied by the formation of anode and cathode spots on the electrode surface. The plasma structures and spots periodically appear and randomly move at the interface between the media in the space between the electrodes. In this case, the temperature increases along the surface of the aluminum anode in a range of 100–180°C (Fig. 3). The random nature of the motion of the studied objects over the electrode surface can be explained by a local change in the electric field due to melting and a change in the topography of the aluminum anode surface.

With an increase in voltage from 600 to 800 V, the rate and nature of the processes occurring at the interface between the media become different. The cone-shaped plasma structures and local spots on the electrode surface merge and transform into a volumetric (diffuse) discharge (Fig. 2b). It is suggested by the analysis of fluctuations in the current strength and discharge voltage that the values of the current strength increase from 0.5 to 11.0 A and the current pulse formation frequency decreases (Fig. 4). The combustion of a volumetric (diffuse) discharge is accompanied by an intense release of convective vapor–air flows, the formation of droplets of various diameters and acoustic pops, the turbulent mixing of the electrolyte, and the perturbation of the solution surface.

749
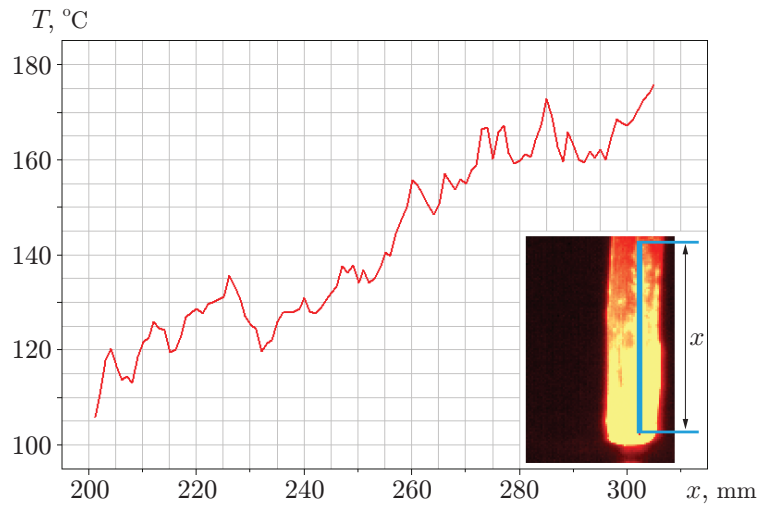
Fig. 3. Heat flux distribution along the aluminum anode during the electric discharge combustion (x denotes the length of the investigated region on the surface of the aluminum anode).
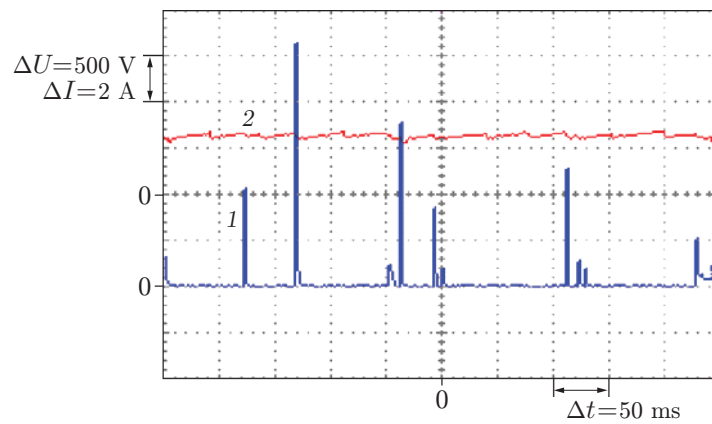

Fig. 4. Oscillograms of fluctuations of the discharge current (*1*) and voltage (*2*).

The change in the dynamics of the processes occurring in the system can be explained by an increase in the power comprised in the discharge. The formation of a high-power discharge results in the processes that are characteristic of an electro-hydraulic explosion with the formation of shock waves, which propagates in the near-electrode space, thereby perturbing and displacing the electrolyte solution from the surface of the aluminum anode. These processes can lead to an increase in the interelectrode distance, discharge damping, and circuit opening. Next, the vapor–air shell collapses and the electrolyte solution interacts with the surface of a highly heated anode, which leads to another breakdown and ignition of the discharge.

It is shown by analyzing the emission spectrum shows that various molecules, ions, and atoms of hydrogen, aluminum, and sodium are present in the plasma section under study. The instrumental broadening in the spectrum under study (the minimum width of the spectral line that the spectrometer can detect) is checked using the Al I atomic line (669.7 nm). The minimum width of optically thin and narrowest lines is $\Delta\lambda_G \approx 1$ nm. This width is taken as the hardware width ($\Delta\lambda_G$ is the half-width of the Gaussian contour). The electron concentration in the plasma is estimated using the half-width of several hydrogen lines in the Balmer series. The measured half-width

750

Voigt and Lorentz profile half-widths and the corresponding values
of the electron density on the hydrogen lines

Hydrogen lines	$\Delta\lambda_V$, nm	$(n_e)_V$, cm^{-3}	$\Delta\lambda_L$, nm	$(n_e)_L$, cm^{-3}
H_α	1.36	$3 \cdot 10^{16}$	0.60	$5.8 \cdot 10^{16}$
H_β	1.59	$2 \cdot 10^{16}$	0.93	$9.4 \cdot 10^{15}$
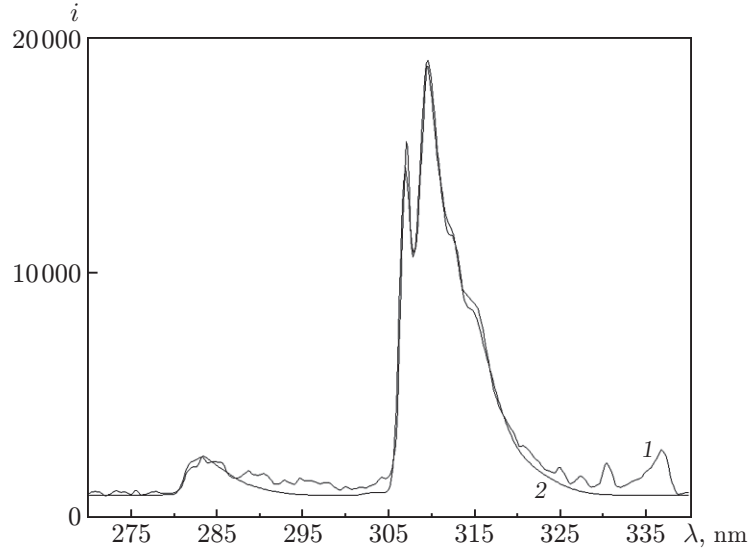
Fig. 5. Experimental (*1*) and model (*2*) spectra for the OH molecular band (*i* is the radiation intensity).

$\Delta\lambda_V$ is 1.36 nm for line H_α and $\Delta\lambda_V = 1.59$ nm for line H_β. With account for the instrumental component, the broadening of the line due to the influence of pressure (the Lorentz half-width) is determined by the equation

$$\Delta\lambda_V \approx 0.5346\,\Delta\lambda_L + \sqrt{0.2166\,\Delta\lambda_L^2 + \Delta\lambda_G^2}\,,$$

where $\Delta\lambda_V$ is the Voigt profile half-width and $\Delta\lambda_L$ is the Lorentz profile half-width.

The electron concentration is determined from the equation given in [22]:

$$n_e = 10^{13}(\Delta\lambda_L)^{3/2}\Big(C_0(T) + \sum_{n=1}^{m} C_n(T)(\ln\Delta\lambda_L)^n\Big).$$

The Lorentz profile half-width is $\Delta\lambda_L = 0.601$ nm for line H_α and $\Delta\lambda_L = 0.93$ nm for line H_β line (see the table). According to [22], $\Delta\lambda_L = 1.36$ nm for line H_α corresponds to an electron density $n_e = 5.8 \cdot 10^{16}$ cm^{-3}, and $\Delta\lambda_L = 0.93$ nm for line H_β corresponds to an electron density $n_e = 9.4 \cdot 10^{16}$ cm^{-3}. According to [23], the half-width of line H_α corresponds to a concentration $n_e = 1.9 \cdot 10^{16}$ cm^{-3}, the half-width of line H_β corresponds to a concentration $n_e = 2 \cdot 10^{16}$ cm^{-3}. As the half-width $\Delta\lambda_V = 1.59$ nm of line H_β is larger than the half-width $\Delta\lambda_V = 1.36$ nm of line H_α, the electron concentration should be determined from line H_β because the contribution of the instrumental function to the half-width of the physical (measured) contour is less significant. Then the electron concentration is $n_e = 9.4 \cdot 10^{16}$ cm^{-3}.

Molecular bands are studied to estimate the vibrational temperature T_ν and rotational temperature T_r of the heavy component. The most clearly defined in the spectrum is the presence of the OH(A–X) molecule (A–X is an allowed electric dipole transition). The temperature analysis is carried out by comparing the experimentally obtained spectrum with the calculated one (Fig. 5). The rotational and vibrational temperatures turn out to be equal to $T_r = 3550$ K and $T_\nu = 4900$ K. The atomic or ionic lines of the spectrum are needed to determine the

electron temperature. In the initial state, the electrolytic cell is filled with electrolyte to a level of 20 mm. The multiphase medium model is applied. Three phases are considered: air, liquid electrolyte, and water vapor. Joule heat release, thermal conductivity, thermal convection, water vaporization, water condensation, surface tension, and processes of hydrogas dynamics are taken into account. When the multiphase medium model is used, the following equations are solved.

—Mixture continuity equation

$$\frac{\partial}{\partial t}\rho_m + \nabla \cdot (\rho_m \boldsymbol{v}_m) = 0,$$

where $\boldsymbol{v}_m$ denotes the mass average velocity of the mixture:

$$\boldsymbol{v}_m = \frac{1}{\rho_m}\sum_{k=1}^{3}\alpha_k \rho_k \boldsymbol{v}_k,$$

ρ_m is the average density:

$$\rho_m = \sum_{k=1}^{3}\alpha_k \rho_k,$$

α_k and ρ_k denote the volume fraction and density of component k:

$$\sum_{k=1}^{3}\alpha_k = 1;$$

— Motion equation (momentum equation)

$$\frac{\partial}{\partial t}(\rho_m \boldsymbol{v}_m) + \nabla \cdot (\rho_m \boldsymbol{v}_m \cdot \boldsymbol{v}_m) = -\nabla p + [\mu_m(\nabla \boldsymbol{v}_m + \nabla \boldsymbol{v}_m^{\mathrm{t}})]$$

$$+ \rho_m \boldsymbol{g} + \boldsymbol{F} + \nabla \cdot \Big(\sum_{k=1}^{3}\alpha_k \rho_k \boldsymbol{v}_{dr,k} \cdot \boldsymbol{v}_{dr,k}\Big),$$

where μ_m is the average viscosity of the mixture:

$$\mu_m = \sum_{k=1}^{3}\alpha_k \mu_k,$$

$\boldsymbol{v}_{dr,k}$ is the drift velocity of component k:

$$\boldsymbol{v}_{dr,k} = \boldsymbol{v}_k - \boldsymbol{v}_m,$$

p is the pressure, $\boldsymbol{g}$ is the acceleration of gravity, and $\boldsymbol{F}$ is the bulk force vector (for example, surface tension);

—Energy equation

$$\frac{\partial}{\partial t}\Big(\sum_{k=1}^{3}\alpha_k \rho_k E_k\Big) + \nabla \cdot \Big(\sum_{k=1}^{3}\alpha_k \boldsymbol{v}_k(\rho_k E_k + p)\Big) = \nabla \cdot (k_{\mathrm{eff}}\nabla T) + S_E, \tag{1}$$

where k_{eff} is the effective thermal conductivity of component k:

$$k_{\mathrm{eff}} = \sum_{k=1}^{3}\alpha_k(k_k + k_t),$$

k_t is the thermal conductivity due to the presence of turbulence and S_E is the bulk density of heat source power.

In Eq. (1), for the specific energy of the gas phase, the following expression is accepted:

$$E_k = h_k - \frac{p}{\rho_k} + \frac{v_k^2}{2}$$

(h_k is the specific enthalpy); for the specific energy of the liquid phase, the following expression is accepted:

$$E_k = h_k.$$

This model takes into account the Joule heat release:

$$S_E = \boldsymbol{j} \cdot \boldsymbol{E} = \sigma E^2. \tag{2}$$

Here $\boldsymbol{j}$ is the current density, $\boldsymbol{E}$ is the electric field strength, and σ is the electrical conductivity of the electrolyte.

The equation of continuity of the electric current is written as

$$\operatorname{div} \boldsymbol{j} = 0,$$

where $\boldsymbol{j} = \sigma \boldsymbol{E}$.

For an electrostatic field, $\boldsymbol{E} = -\operatorname{grad} \varphi$, so the equation for the electric field potential takes the form

$$\operatorname{div}(\sigma \operatorname{grad} \varphi) = 0.$$

The following boundary conditions are accepted for Eq. (2): $\varphi = 0$ on the lower conductive plate and $\varphi = U$ on the metal electrode (U is the applied voltage). The Neumann condition $\partial \varphi / \partial n = 0$, which corresponds to the condition of no current flow, is accepted on the side dielectric walls.

The condition of convective heat exchange with the surrounding atmospheric air is set on the vertical side walls for the energy equation, the air pressure is equal to $p_0 = 105$ Pa, and the temperature is $T_a = 300$ K.

Convective heat transfer is described by the Newton–Richmann equation

$$q = \alpha(T_a - T_w),$$

where q is the heat flux density, α is the heat transfer coefficient, and T_w is the wall temperature.

The following criteria are used to determine α:
—Prandtl number

$$\Pr = \frac{\nu}{a} \tag{3}$$

(ν is the kinematic viscosity of air, $a = k/(c_p \rho)$ is the thermal diffusivity, c_p is the heat capacity of air at a constant pressure, ρ is the air density, and k is the thermal conductivity);
—Grashof number

$$\mathrm{Gr} = \frac{g l^3 \beta \, \Delta T}{\nu^2} \tag{4}$$

(l is the height of the vertical wall, β is the air volume expansion coefficient, and $\Delta T = T_a - T_w$);
—Nusselt number determining the convection near a vertical wall:

$$\mathrm{Nu} = 0.75 (\mathrm{Gr} \, \Pr)^{0.25}. \tag{5}$$

The heat transfer coefficient

$$\alpha = \frac{\mathrm{Nu} \, k}{l} \tag{6}$$

for this model is equal to $14 \ \mathrm{W/(m^2 \cdot K)}$.

At the upper boundary of the computational domain, the constant pressure condition $p = p_0$ is accepted, and the particles of the medium can freely cross this surface due to convection.

In calculating the electrical parameters, the value of the specific electrical conductivity of the 3% NaCl solution is taken as equal to $\sigma = 0.54$ S/m. Figure 6 shows the calculated equipotential electric field lines at an electrode voltage $U = 600$ V, and Fig. 7 shows the dependence of the electric field intensity modulus on the vertical coordinate y along the axis of symmetry of the discharge. Near the electrode, the electric field strength reaches $E \approx 150$ kV/m. As the current flows, there is local heating of the electrolyte near the electrode, which leads to the formation of vapor bubbles.

The characteristic vaporization time τ caused by the Joule heat release (2) is estimated as follows. With the heat capacity and thermal conductivity neglected, all the released power is spent on vaporization:
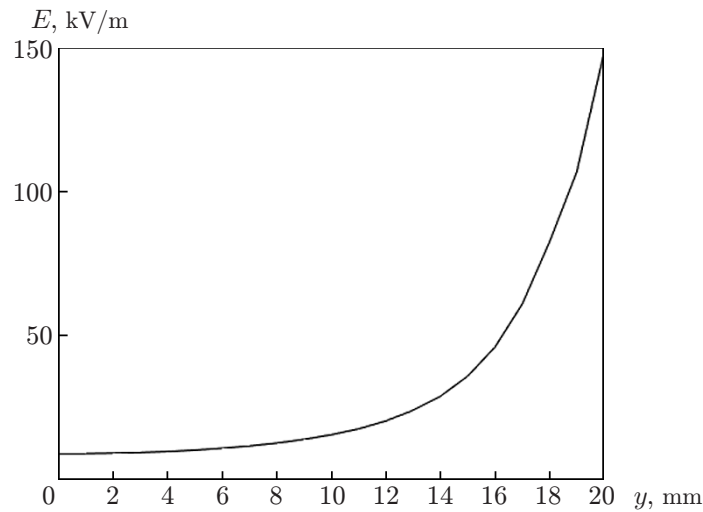
$$S_E \, \Delta V \, \tau = r \rho \, \Delta V.$$

Here r is the specific heat of vaporization, ρ is the water density, and ΔV is the small volume of the electrolyte. Thus, $\tau = r\rho/(\sigma E^2) \approx 0.2$ s.
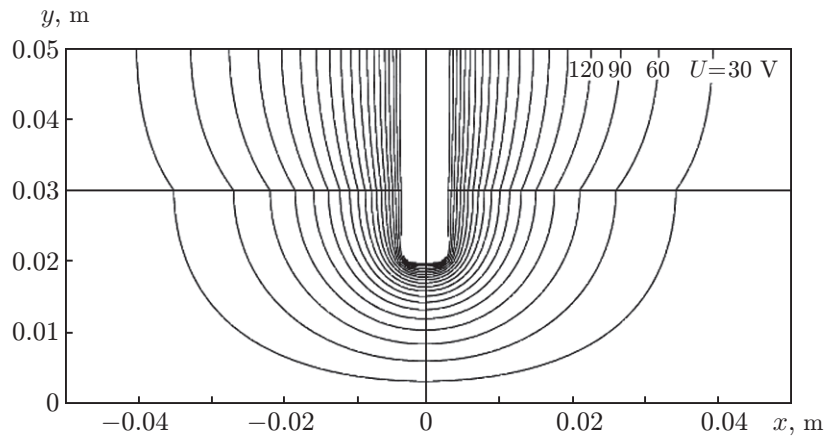
**Fig. 6.** Equipotential electric field lines in a vertical section passing through the axis of symmetry.

Fig. 7. Electric field strength modulus versus the y coordinate along the axis of symmetry of the discharge.

Figure 8 shows the electrolyte and vapor regions at different times. First, bubbles form near the lower edge of the electrode, where the field strength and, consequently, the bulk density of the released power reach their maximum values (Fig. 8a). Subsequently, the vapor covers the submerged part of the electrode, which reduces the area of the contact region with the electrolyte (Figs. 8b and 8c). Then, due to convection, a vertically directed flow of vapor and liquid appears near the electrode, which leads to an increase in the area of the contact region with the electrolyte (Fig. 8d).

The change in the area of the electrolyte contact region with the immersed electrode causes current pulsations (Fig. 9). In a range $t = 1.5–2.0$ s, the area of the contact region of the metal electrode with the electrolyte is maximum, which corresponds to the maximum values of the current strength. Next, the dynamic processes occurring at the boundary of the electrode interaction region (Fig. 8) cause periodic changes in the area of this region, thereby causing a decrease and increase in the current strength in a time interval $t = 2.40–3.75$ s. The characteristic time of current pulsations approximately coincides with the calculated value $\tau \approx 0.2$ s.

754
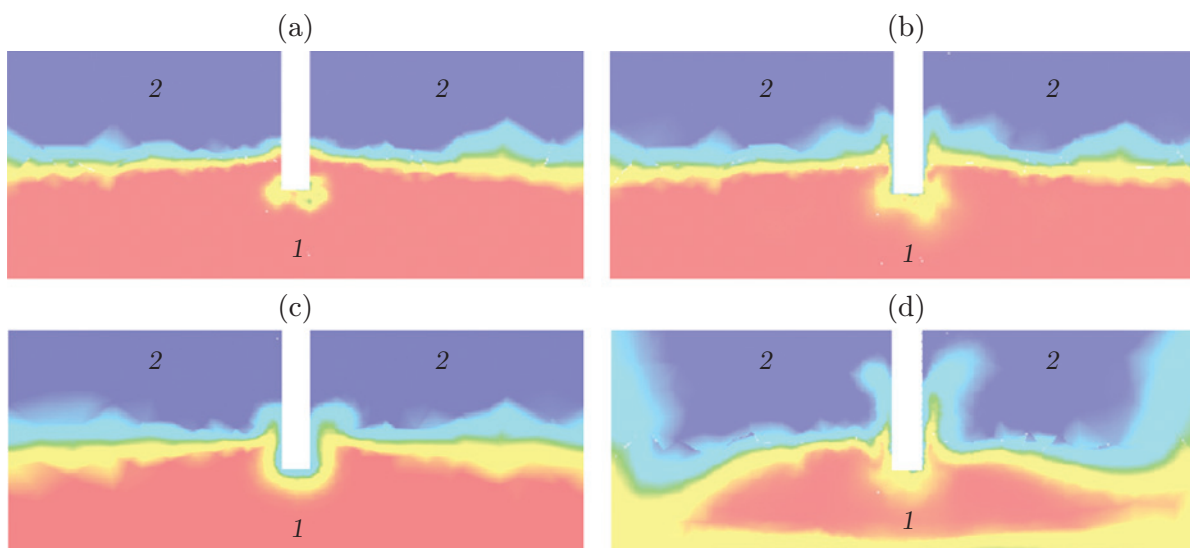
Fig. 8. Electrolyte region (*1*) and vapor region (*2*) at $t = 1.6$ (a), 2.0 (b), 2.4 (c), and 2.6 s (d).
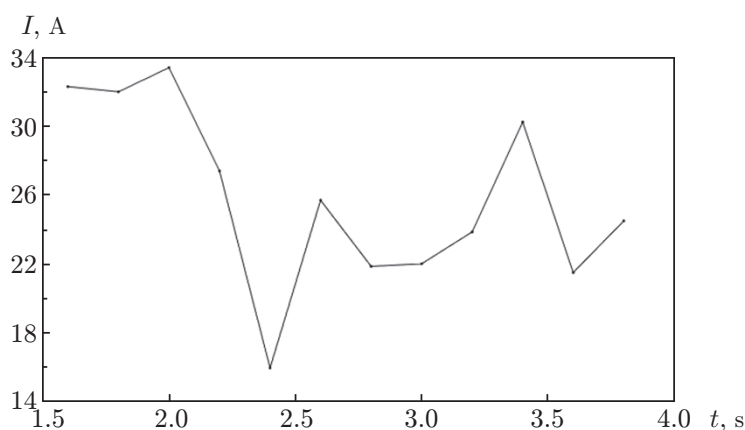
Fig. 9. Estimated dependence of the current strength between the anode and the copper plate (see Fig. 1) on time.

CONCLUSIONS

The following results are obtained in the study performed.

The formation of cone-shaped plasma microchannels and the formation of anode and cathode spots on the electrode surface in a voltage range of 200–500 V are revealed. As the voltage increases from 600 to 800 V, a discharge is formed in the form of current pulses in a range of 0.2–11.0 A.

It is established that various atoms and molecules are present in the discharge spectrum. The electron density obtained from the broadening of line H_β is $n_e = (9.4 \pm 0.4) \cdot 10^{16}$ cm^{-3}. The rotational and vibrational temperatures of the hydroxyl OH molecule are $T_r = 3550$ K and $T_\nu = 4900$ K, respectively.

The results of numerical simulation of the current flow in the electrolytic cell and the initial stage of the discharge are presented.

The obtained results can be used to develop mathematical models of plasma–liquid systems with the considered electrode configuration, as well as to create plasma devices for treating the surfaces of aluminum metal products.

REFERENCES

1. P. Bruggerman, M. J. Kushner, B. R. Locke, et al., "Plasma–Liquid Interactions: A Review and Roadmap," Plasma Sources Sci. Technol. **25**, 053002 (2016).
2. Al. F. Gaisin, E. E. Son, A. V. Efimov, et al., "Spectral Diagnostics of Plasma Discharge between a Metal Cathode and Liquid Anode," High Temp. **55**, 457–460 (2017).
3. N. Kashapov, R. Kashapov, and L. Kashapov, "Influence of the Electrolytic Cathode Temperature on the Self-Sustaining Mechanism of Plasma-Electrolyte Discharge," J. Phys. D: Appl. Phys. **51**, 494003 (2018).
4. Y. Sakiyama, D. B. Graves, H.-W. Chang, et al., "Plasma Chemistry Model of Surface Microdischarge in Humid Air and Dynamics of Reactive Neutral Species," J. Phys. D: Appl. Phys. **45**, 425201 (2012).
5. Y. P. Raizer and J. E. Allen, *Gas Discharge Physics* (Springer, Berlin, 1997).
6. E. I. Meletis, X. Nie, F. L. Wang, and J. Jiang, "Electrolytic Plasma Processing for Cleaning and Metal-Coating of Steel Surfaces," Surf. Coat. Technol. **150**, 246–256 (2002).
7. T. Ishijima, K. Nosaka, Y. Tanaka, et al., "A High-Speed Photoresist Removal Process Using Multibubble Microwave Plasma under a Mixture of Multiphase Plasma Environment," Appl. Phys. Lett. **103**, 142101 (2013).
8. Al. F. Gaisin, "Investigation of the Effect of a Low-Temperature Plasma of Vapor–Gas Discharges with the Use of Electrolytic Electrodes at Lower Pressure on Products of Complex Shape," Inorgan. Materials: Appl. Res. **8**, 392 (2017).
9. Al. F. Gaysin, A. Kh. Gil'mutdinov, and D. N. Mirkhanov, "Electrolytic-Plasma Treatment of the Surface of a Part Produced with the Use of Additive Technology," Metal Sci. Heat Treatment **60**, 128–132 (2018).
10. R. Kashapov, L. Kashapov, and N. Kashapov, "Research of Plasma-Electrolyte Discharge in the Processes of Obtaining Metallic Powders," J. Phys.: Conf. Ser. **927**, 012086 (2017).
11. R. Wüthrich and A. Allagui, "Building Micro and Nanosystems with Electrochemical Discharges," Electrochimica Acta **55**, 8189–8196 (2010).
12. K. T. Abdul and A. A. Kaliani, "Glow Discharge Plasma Electrolysis for Nanoparticles Synthesis," Ionics **18**, 315–327 (2012).
13. G. Saito, S. Hosokai, M. Tsubota, and T. Akiyama, "Synthesis of Copper/Copper Oxide Nanoparticles by Solution Plasma," J. Appl. Phys. **110**, 023302 (2011).
14. T. Paulmier, J. M. Bell, and P. M. Fredericks, "Deposition of Nano-Crystalline Graphite Films by Cathodic Plasma Electrolysis," Thin Solid Films **515**, 2926–2934 (2007).
15. C. Quan and Y. He, "Properties of Nanocrystalline Cr Coatings Prepared by Cathode Plasma Electrolytic Deposition from Trivalent Chromium Electrolyte," Surface Coatings Technol. **269**, 319–323 (2015).
16. P. Mezei, T. Czerfalvi, M. Janossy, et al., "Similarity Laws for Glow Discharges with Cathodes of Metal and an Electrolyte," J. Phys. D: Appl. Phys. **31**, 2818 (1998).
17. M. Smoluch, P. Mielczarek, and J. Silberring, "Plasma-Based Ambient Ionization Mass Spectrometry in Bioanalytical Sciences," Mass Spectrom. Rev. **35**, 22–34 (2016).
18. K. H. Becker, K. H. Schoenbach, and J. G. Eden, "Microplasmas and Applications," J. Phys. D: Appl. Phys. **39**, R55 (2006).
19. E. E. Son, R. Sh. Sadriev, Al. F. Gaisin, et al., "Peculiarities of Microwave Discharge between a Copper Pin Electrode and Technical Water," High Temp. **52**, 939 (2014).
20. P. Bruggeman and C. Leys, "Non-Thermal Plasmas in and in Contact with Liquids," J. Phys. D: Appl. Phys. **42**, 053001 (2009).
21. S. Samukawa, M. Hori, Sh. Rauf, et al., "The 2012 Plasma Roadmap," J. Phys. D: Appl. Phys. **45**, 253001.
22. G. A. Kasabov and V. V. Eliseev, *Spectroscopic Tables for Low-Temperature Plasma: Manual* (Atomizdat, Moscow, 1973) [in Russian].
23. V. N. Ochkin, *Spectroscopy of Low-Temperature Plasma* (Fizmatlit, Moscow, 2006) [in Russian].